

**Space-time properties of Gram-Schmidt vectors in classical Hamiltonian evolution**Jason R. Green,<sup>1,2,3,\*</sup> Julius Jellinek,<sup>2,†</sup> and R. Stephen Berry<sup>3,‡</sup><sup>1</sup>*Department of Chemistry, University of Cambridge, Lensfield Road, Cambridge CB2 1EW, United Kingdom*<sup>2</sup>*Chemical Sciences and Engineering Division, Argonne National Laboratory, Argonne, Illinois 60439, USA*<sup>3</sup>*Department of Chemistry and The James Franck Institute, The University of Chicago, Chicago, Illinois 60637, USA*

(Received 5 May 2009; published 14 December 2009)

Not all tangent space directions play equivalent roles in the local chaotic motions of classical Hamiltonian many-body systems. These directions are numerically represented by basis sets of mutually orthogonal Gram-Schmidt vectors, whose statistical properties may depend on the chosen phase space-time domain of a trajectory. We examine the degree of stability and localization of Gram-Schmidt vector sets simulated with trajectories of a model three-atom Lennard-Jones cluster. Distributions of finite-time Lyapunov exponent and inverse participation ratio spectra formed from short-time histories reveal that ergodicity begins to emerge on different time scales for trajectories spanning different phase-space regions, in a narrow range of total energy and history length. Over a range of history lengths, the most localized directions were typically the most unstable and corresponded to atomic configurations near potential landscape saddles.

DOI: [10.1103/PhysRevE.80.066205](https://doi.org/10.1103/PhysRevE.80.066205)

PACS number(s): 05.45.Pq, 31.15.xv, 82.20.Wt, 05.45.Jn

**I. INTRODUCTION**

How do classical Hamiltonian systems explore their accessible phase space? As the history of a chaotic trajectory fills a phase-space volume, it tends toward equilibrium, presumably becoming increasingly ergodic, perhaps becoming fully ergodic. It is possible, in such an evolution, for distinct regions of phase space to become filled on different time scales, each region separately tending to local ergodicity [1–5]. In this paper, we ask what are the statistical properties of the tangent space directions important to the approach toward local ergodicity in each phase-space region? Specifically, how spatially localized or delocalized and stable or unstable are these tangent space directions? The answers will likely be sensitive to the phase space visited, the chosen time scale, the number of conserved quantities, the types of dynamics, the local and regional topography of the potential-energy surface, and, in general, the initial conditions [6–10]. Thus, we will seek to answer these questions for a range of total energies, time scales, and initial conditions, relating these directions and their properties to features of the potential-energy landscape.

The Kolmogorov-Sinai entropy [2,8,9,11], power spectra [12], and, more recently, coherence times, measuring the time needed for chaotic behavior to develop [13] are examples of quantities that have proven useful in previous studies of Hamiltonian systems. Our strategy to answer the questions above will make use of Lyapunov exponent spectra [6] and inverse participation ratios [14]. Over a chosen time span, a finite-time Lyapunov exponent measures the degree of chaos or instability, the time-average rate at which a small initial perturbation diverges or converges along a dynamical trajectory. In practical calculations, such as those presented here, they are estimated from a basis set of tangent vectors

chosen to numerically represent these perturbations along the trajectory. Often, periodic application of the Gram-Schmidt (GS) procedure is used to impose orthogonality on the basis [15,16]. For a sufficiently long trajectory and time  $t$ , the basis becomes independent of the initial phase point at  $t=0$  [17]. At subsequent times, the GS vectors (GSVs) belonging to this GS basis define mutually orthogonal maximally changing directions, at which initially close trajectories diverge at exponential rates [18–20].

A GS basis is propagated concurrently with the trajectory, but according to a linearized variational equation of motion [18]. After finite-time histories, GSVs are local estimates of the Lyapunov vectors and their time-average rates of expansion or contraction are estimates of the Lyapunov exponents. However, orthogonality is not a geometric property of the intrinsic local vector set in tangent space or the linearized dynamics. Consequently, orthogonal bases are not covariant under these dynamics [21]. Nevertheless, for practical purposes [15,16], the GS basis is a convenient and common tangent vector set [22,23]. As the GSVs evolve in time, they change direction and magnitude, so GSV directions important in a given finite-time segment of a trajectory may not be the same as those in the asymptotic limit or even other finite-time spans.

To access finite-time spans, we partition trajectories into uniform time segments. Distributions of properties collected from the segments then characterize the trajectory. Finite-time Lyapunov exponent distributions are invariants of the dynamical system for an infinitely long trajectory: they must be independent of the trajectory or initial condition [24] because of Oseledec's theorem [25]. We calculate finite-time Lyapunov exponent as well as inverse participation ratio distributions of the GSV set for the same time history segments. The inverse participation ratio is a rough estimate of the inverse number of components contributing to each GSV on average, in a time segment. We simultaneously quantify localization and chaos with these distributions, probing the tangent space dynamics as the trajectory visits different phase-space locales.

\*[jg525@cam.ac.uk](mailto:jg525@cam.ac.uk)†[jellinek@anl.gov](mailto:jellinek@anl.gov)‡[berry@uchicago.edu](mailto:berry@uchicago.edu)

In the work of Amitrano *et al.*, trajectories of the Lennard-Jones trimer were partitioned and distributions of the maximal Lyapunov exponent were calculated for a range of segment lengths [3–5]. At total energies just high enough to allow passage over the linear configuration saddles, motion in phase space separated into a region of highly chaotic behavior, characterizing motion in the potential well, and a region with much more regular dynamics, characterizing motion across the saddle [11,26,27]. Bimodal exponent distributions were observed [4] over a range of total energy and time segment length, indicating the two regions of phase space have separable time scales for the emergence of ergodicity.

Amitrano *et al.* left open the question of what tangent space directions are important in achieving ergodicity in these two phase-space regions at total energies where there is a separation of time scales [4]. Distributions of the inverse participation ratios and finite-time exponents for the GS basis provide us with insight into the degree of localization and chaos in the tangent space directions responsible for the time scale separation in those phase-space regions. We extract these statistical GSV properties from simulations of the classical constant-energy trajectories of the same model three-atom cluster bound by pairwise-additive Lennard-Jones potentials.

Whether regular or chaotic, Hamiltonian dynamics are often interpreted as a response to the topographical features of the underlying potential-energy landscape [9]. Even in large systems, many stationary points of the potential landscape and their normal modes are often known [28]. While the normal modes of these stationary points are inadequate to completely describe the dynamics, they provide us with a systematic means of probing the dependence of the dynamics on initial conditions and total energy. The present analysis of a small prototypical atomic cluster is intended to be a proof-of-principle study of Hamiltonian systems with many degrees of freedom [29–34].

## II. MODEL AND COMPUTATIONAL METHODOLOGY

To describe the triatomic cluster, we chose the center-of-mass reference frame, the Cartesian coordinate system, and the classical Lennard-Jones Hamiltonian

$$H(\mathbf{q}, \mathbf{p}) = \frac{1}{2m} \sum_{i=1}^n \mathbf{p}_i^T \mathbf{p}_i + 4\epsilon \sum_{i<j}^n \left\{ \frac{\sigma^{12}}{|\mathbf{r}_{ij}|^{12}} - \frac{\sigma^6}{|\mathbf{r}_{ij}|^6} \right\}, \quad (1)$$

where  $|\mathbf{r}_{ij}| = |\mathbf{q}_i - \mathbf{q}_j|$  is the Euclidean distance between atoms  $i$  and  $j$  in terms of their positions and  $n=3$  is the number of atoms. In reduced units, the atomic positions are in units of the distance  $\sigma$  at which the repulsive and attractive terms are equal, the time  $t = \sqrt{m\sigma^2/\epsilon}$  is in the natural unit based on  $\sigma$ , the mass  $m$ , and the pair well depth  $\epsilon$ , and energies are in units of  $\epsilon$ . Choosing these units sets  $m=1$ ,  $\sigma=1$ , and  $\epsilon=1$ .

Let us denote a phase point as  $\mathbf{x} = (\mathbf{q}, \mathbf{p})^T \in \mathbb{R}^{2s}$ , where  $\mathbf{x}$  is composed of all positions  $\mathbf{q} \in \mathbb{R}^s$  and their linear momenta  $\mathbf{p} \in \mathbb{R}^s$ , and  $s=3n$  is the number of position coordinates. Initially, the total energy  $H(\mathbf{q}, \mathbf{p}) = E$  was localized in one of the three normal vibrational modes of the global minimum, equilateral triangular configuration (Fig. 1), or one of the two

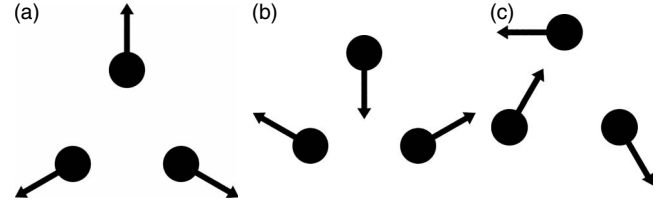


FIG. 1. Three normal vibrational modes of the global potential minimum equilateral triangle  $D_{3h}$  of the Lennard-Jones trimer. At the potential minimum, bond angles are  $60^\circ$  and bond lengths are  $\sqrt[3]{2}\sigma$ . Vectors indicate atomic displacements of the (a)  $A_1'$ , (b) symmetric  $E'$ , and (c) asymmetric  $E'$  modes. We call these the symmetric stretch, symmetric  $E'$ , and asymmetric  $E'$ . The  $E'$  modes are symmetric or asymmetric with respect to the vertical mirror plane.

modes of the linear configuration (Fig. 2).

These modes were defined by the eigenvectors of the Hessian matrix. The initial configuration was distorted by stepping the configuration-space vector  $\mathbf{q}(t_0)$  of the equilibrium geometry in the Hessian eigenvector direction with the least nonzero increase in potential energy. After each configuration-space step, the potential energy fixed the total energy for the subsequent trajectory.

Initial excitations and atomic motion are restricted to a two-dimensional plane. The initial conditions  $\mathbf{x}(t_0)$  also fixed the center of mass, linear momentum, and angular momentum at zero, and they remained zero during the simulations. Individual trajectories  $\{\mathbf{x}(t_j) : 0 < j < L\}$  were propagated over  $L$  time steps according to Hamilton's equations using the “velocity Verlet” algorithm [35–37]. The total energy was conserved up to one part in  $10^5$  for millions of time steps. Each time step was  $\tau = t_{j+1} - t_j = 10^{-3}$  in reduced units.

A basis set of arbitrary orthonormal vectors,  $\{\mathbf{u}_i(t_0)\}$ ,  $i=1, \dots, 2s$  was defined at the initial phase point  $\mathbf{x}(t_0)$ . The  $2s \times 2s$  identity matrix was used here. At all times, the phase point  $\mathbf{x}(t)$  was taken to be the origin of the basis' reference frame. This is a basis of the tangent space, a vector space, at each point along the trajectory. When propagated in time, fixed to the phase point, this vector set becomes the GS basis  $\{\mathbf{g}_i(t)\}$  at time  $t$ .

Members  $\mathbf{g}$  of the basis, the GSVs, are variations in the form  $(\delta\mathbf{q}, \delta\mathbf{p})^T \in T\mathbb{R}^{2s}$ , where  $\delta\mathbf{q}, \delta\mathbf{p} \in T\mathbb{R}^s$ . They are numerically propagated concurrently with the phase point, according to the linearized variational equation of motion, with the discretized algorithm

$$\begin{pmatrix} \delta\mathbf{q}(t_j) \\ \delta\mathbf{p}(t_{j+1/2}) \end{pmatrix} = \mathbf{A} \begin{pmatrix} \delta\mathbf{q}(t_j) \\ \delta\mathbf{p}(t_j) \end{pmatrix}, \quad (2)$$

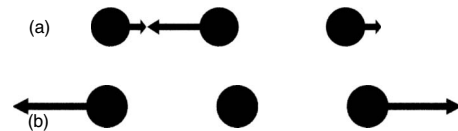


FIG. 2. The two normal vibrational modes of the linear configuration  $D_{\infty h}$  of the Lennard-Jones trimer. Bond lengths are  $\sqrt[3]{2}\sigma$ . Vectors indicate atomic displacements of the (a) the asymmetric and (b) the symmetric stretches.

$$\begin{pmatrix} \delta\mathbf{q}(t_{j+1}) \\ \delta\mathbf{p}(t_{j+1/2}) \end{pmatrix} = \mathbf{B} \begin{pmatrix} \delta\mathbf{q}(t_j) \\ \delta\mathbf{p}(t_{j+1/2}) \end{pmatrix}, \quad (3)$$

$$\begin{pmatrix} \delta\mathbf{q}(t_{j+1}) \\ \delta\mathbf{p}(t_{j+1}) \end{pmatrix} = \mathbf{C} \begin{pmatrix} \delta\mathbf{q}(t_{j+1/2}) \\ \delta\mathbf{p}(t_{j+1/2}) \end{pmatrix}. \quad (4)$$

The tangent space propagators for each step  $\mathbf{A}$ ,  $\mathbf{B}$ , and  $\mathbf{C}$  are the matrices

$$\mathbf{A} = \begin{pmatrix} \mathbf{I} & \mathbf{0} \\ -\frac{\tau}{2}\mathbf{H}(t_j) & \mathbf{I} \end{pmatrix}, \quad (5)$$

$$\mathbf{B} = \begin{pmatrix} \mathbf{I} & \mathbf{T} \\ \mathbf{0} & \mathbf{I} \end{pmatrix}, \quad (6)$$

$$\mathbf{C} = \begin{pmatrix} \mathbf{I} & \mathbf{0} \\ -\frac{\tau}{2}\mathbf{H}(t_{j+1}) & \mathbf{I} \end{pmatrix}, \quad (7)$$

composed of  $s \times s$  blocks, where  $\tau = t_{j+1} - t_j$  is the time step size,  $(\mathbf{T})_{kl} = \tau \delta_{kl} / m_k$ ,  $\delta_{kl}$  is the Kronecker delta,  $\mathbf{I}$  is the identity matrix, and  $\mathbf{H}$  is the mass-weighted Hessian matrix. A  $\tau$  of  $10^{-3}$  in reduced units was also used in this algorithm, the linearized form of the velocity Verlet algorithm that propagated the trajectory.

The tangent space propagator for a complete time step  $\mathbf{M}$  is the matrix product of the propagators for each step of the algorithm  $\mathbf{M} = \mathbf{CBA}$ . A complete time step of the GS vectors is then

$$\bar{\mathbf{g}}_i(t_{j+1}) = \mathbf{M}(t_{j+1}, t_j) \mathbf{g}_i(t_j). \quad (8)$$

Following each time step, the GSVs are still a tangent space basis but are no longer orthogonal; nonorthogonal GSVs are denoted by  $\bar{\mathbf{g}} = (\delta\mathbf{q}, \delta\mathbf{p})^T \in TR^{2s}$ , where  $\delta\mathbf{q}, \delta\mathbf{p} \in TR^s$ . That is, the integrated linearized equation of motion is not an orthogonal mapping [21]. Thus, at regular intervals during the trajectory, we applied the GS orthogonalization procedure to  $\{\bar{\mathbf{g}}_i\}$ .

Propagation orients the first GSV parallel to the maximally changing tangent space direction. Propagation with periodic orthogonalization orients the remaining  $\mathbf{g}_i$  in the maximally changing direction of a subspace of tangent space, orthogonal to all subspaces  $k < i$ ,  $k = 1, \dots, i-1$ . Over each  $5 \times 10^7$  time step trajectory, we propagated a GS basis and orthonormalized it every 10 steps. Applications of the GS procedure generated  $\{\mathbf{g}_i\}$  and the Euclidean norms  $\{\|\mathbf{g}_i\|\}$ . The norms were stored but also used to normalize the GS basis to prevent arithmetic overflow.

Asymptotic estimates of Lyapunov exponent spectra were obtained from the GS bases propagated with trajectories. Each Lyapunov exponent  $\lambda_i$  was calculated from the Euclidean norm  $\|\mathbf{g}_i(t)\|$  stored after GS orthogonalization of each GS basis vector. In natural logarithmic units (nats) per reduced time, the estimated exponents are

$$\lambda_i(t_L) \equiv \langle \ln \|\mathbf{g}_i(t_j)\| \rangle_{t_L}, \quad (9)$$

where  $\langle \cdot \rangle_{t_L}$  is a time average over the interval  $0 \leq j \leq L$ . Lyapunov exponents  $\lim_{L \rightarrow \infty} \lambda_i(t_L) \equiv \lambda_i$  sum to zero for Hamiltonian systems and given  $M$  constants of motion, at least  $2M$  exponents are zero [38]. The numerical procedure estimates exponents in this limit by averaging the logarithm of  $\|\mathbf{g}_i\|$  over the time interval  $[0, t_L]$ .

The Lennard-Jones trimer, simulated in a reference frame with its origin fixed at the center of mass, has seven constants of motion: total energy, three components of total linear momentum, and three components of total angular momentum. Consequently, as was confirmed in our simulations, at most four exponents may be nonzero. Furthermore, each positive exponent has a corresponding negative exponent of equal magnitude forming a conjugate, or Smale, pair [39]. Exponents listed in descending order are typically numbered by indices  $\lambda_1 \geq \lambda_2 \geq \dots \geq \lambda_{2s}$ . Each exponent  $\lambda_i$ ,  $1 \leq i \leq s$  has a conjugate  $\lambda_{2s-i+1}$ , together forming a conjugate pair related by  $\lambda_i = -\lambda_{2s-i+1}$  [40].

Following normalization, GSV structure was probed with a modified mean inverse participation ratio  $Y$ . Over the entire trajectory of length  $L$ , this ratio measures localization of the GSVs [22,23,41] in the union of tangent spaces associated with the trajectory. It was originally used to gauge the degree of localization of normal modes in the configuration space of condensed phase systems [14]. For the  $i$ th GSV, we take the mean inverse participation ratio to be

$$Y_i = \left\langle N^2 \sum_{k=1}^s [g^{ki}(t_j)]^4 \right\rangle, \quad (10)$$

where  $g^{ki}$  is the  $k$ th component of  $i$ th GSV,  $(g^{ki})^2 \equiv (\delta q^{ki})^2 + (\delta p^{ki})^2$ , the brackets indicate an average over the number of time steps in a trajectory (or trajectory segment), and the normalization factor  $N$  is  $1 / \sum_{k=1}^s [g^{ki}(t_j)]^2 = 1$ . Evaluating  $\{Y_i\}$  gives a rough estimate of the average inverse number of components contributing to each GSV over the trajectory or trajectory segment. On average, a normalized purely delocalized GSV would have all components equal to  $1/\sqrt{2s}$ , while a normalized purely localized GSV would have one nonzero component equal to unity. Hence, a localized GSV has a  $Y$  nearer unity and a delocalized GSV has a  $Y$  nearer  $1/s$ . Indices correspond to the associated GSV and Lyapunov exponent.

### III. NUMERICAL RESULTS AND ANALYSIS

Dynamical trajectories may be interpreted as a response to configurational motion on the potential-energy landscape. So before describing our results from simulated trajectories, we examine the features of the landscape using the vibrational modes in Fig. 1 as ‘‘coordinates.’’ From Fig. 1(a), symmetrically stretched configurations are equilateral triangles, preserving  $C_{3v}$  symmetry. The potential energy at the origin of each map in Fig. 3 is that of a symmetrically stretched configuration,  $V = -3.0\epsilon$ ,  $-2.431\epsilon$ ,  $-1.673\epsilon$ , and  $-1.114\epsilon$  for Figs. 3(a)–3(d).

Geometries away from the equilateral triangles do not have  $D_{3h}$  symmetry. Thus, points off the origin on a map are

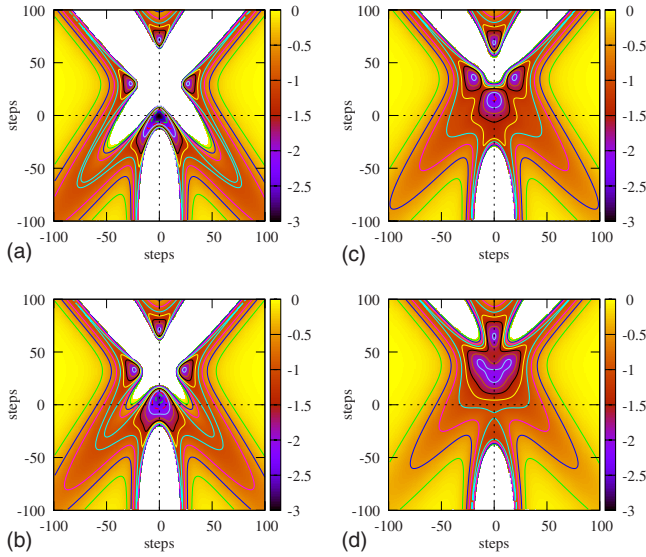


FIG. 3. (Color online) Potential-energy level curves in the interval  $-3.0\epsilon \leq V \leq 0.0\epsilon$  for linear combinations of the three vibrational modes of the trimer. Axes mark the integer number of steps in scaled Hessian eigenvector directions of the asymmetric  $E'$  mode (horizontal axes) and the symmetric  $E'$  mode (vertical axes). At the origin, in the center of each plot, are equilateral triangle configurations of the symmetric stretch. Their potential energies are (a)  $V = -3.0\epsilon$ , (b)  $-2.431\epsilon$ , (c)  $-1.673\epsilon$ , and (d)  $-1.114\epsilon$ . Curves in a given panel are separated by  $\Delta V = 0.25\epsilon$ . White areas are where  $V > 0.0$  and are energetically inaccessible.

potential energies of distinct atomic configurations, linear combinations of the other two modes for the given symmetric stretch configuration. The other two modes of the global minimum equilateral triangle correspond to the  $D_{3h}$  point group [Figs. 1(b) and 1(c)]: one is symmetric and the other is asymmetric with respect to the vertical plane that includes the  $C_3$  axis. To simplify visualization of the potential landscape, we take a configuration of the symmetric stretch and map the potential energy of configurations that are a combination of these two  $E'$  modes. Configurations of the symmetric  $E'$  mode preserve  $C_{2v}$  symmetry and those of the asymmetric mode preserve  $C_s$  symmetry.

Symmetric stretch configurations were found by adding the scaled Hessian eigenvector, to the global minimum configuration. Similarly, to map each cross section of  $E'$  configuration space, the  $E'$  Hessian eigenvectors were scaled and added to the equilateral triangle configuration. Each axis is labeled by the number of steps taken from the origin in eigenvector directions. Vertical lines correspond to the potential energies of the symmetric  $E'$  mode configurations only. Atomic configurations along vertical lines include the equilateral triangles: one located at the origin and isosceles triangles on both sides of the linear configuration. Horizontal lines correspond to the potential energies of the asymmetric  $E'$  mode only. Level curves represent the configurations with the same potential energy.

In Fig. 3(a), the origin is the global minimum equilateral triangle configuration. As the symmetric stretch is excited, the equilateral triangle becomes larger. The origin changes

between Figs. 3(b) and 3(c) from being part of a stable locus, close to the global minimum, to being part of an unstable locus: the equilateral triangle configuration becomes less stable with respect to the other two modes for larger symmetric excitations. Off the vertical axis all four maps, have local minima that are isosceles triangles.

Since the “coordinates” of these maps will be initial conditions for trajectories, their basic features will provide context for the trajectory results presented next. Of particular note are the regions of the potential landscape off the vertical axis that can only be explored by trajectories when the asymmetric  $E'$  mode is active. All the trajectories we simulated were below the threshold energy for evaporation of atoms (an approximate range of  $-3.0\epsilon \leq E \leq -1.0\epsilon$ ). For reference, the linear configuration stationary point has an energy of  $-2.031\epsilon$ . Before analyzing the local space and time properties of these trajectories over this range of total energies, we first examine their long-time properties.

### A. Global properties of phase space

Asymptotic estimates of Lyapunov exponents and inverse participation ratios versus total energy are shown in Fig. 4. Each panel contains results for trajectories, in which the total energy was initially deposited into one of the equilateral triangle modes (Fig. 1). From these trends, we confirm that the Lyapunov exponents  $\lambda_1$  and  $|\lambda_{18}|$  are a conjugate pair, as are  $\lambda_2$  and  $|\lambda_{17}|$ . Each member of a pair varies identically as a nonmonotonic function of total energy, in all three cases. The inverse participation ratio pairs  $Y_1, Y_{18}$  and  $Y_2, Y_{17}$  also vary identically and nonmonotonically with the total energy above the threshold for chaos. These long time or global results demonstrate a dependence on the initially activated mode and its degree of activation. As is especially clear from Figs. 4(a) and 4(c), there are four distinct regions of globally chaotic behavior, chaotic dynamics being detectable in the lowest nonregular region  $-2.5\epsilon < E < -2.1\epsilon$ .

The threshold energy for the onset of chaos was largest when the symmetric stretch was initially excited. We found that in these trajectories, the symmetric stretch first coupled with the symmetric  $E'$  mode (and vice versa). Symmetric stretching motion alone would have restricted geometries along a trajectory to equilateral triangles. In this case, the onset of chaos must be a consequence of mode coupling caused by accumulation of numerical error over time. Which modes ultimately couple during a trajectory depend on the numerical error accumulated, initial mode excited, total energy, symmetry, and potential landscape. In the trajectories giving the results of Fig. 4(b), the initial configuration corresponded to an excitation of the asymmetric  $E'$  mode, which first coupled with the symmetric  $E'$  mode.

Excitation of any one mode in Fig. 1 gave trajectory results with similar trends in the lowest-energy region. For all three initially excited modes, Lyapunov exponents  $\lambda_1$  and  $|\lambda_{18}|$  increase with total energy. We interpret this feature of the curves to be a consequence of the larger accessible phase-space volumes visited in the trajectory’s history; from the potential landscape cross-sections Figs. 3(a) and 3(b), we see that the global minimum potential well broadens along

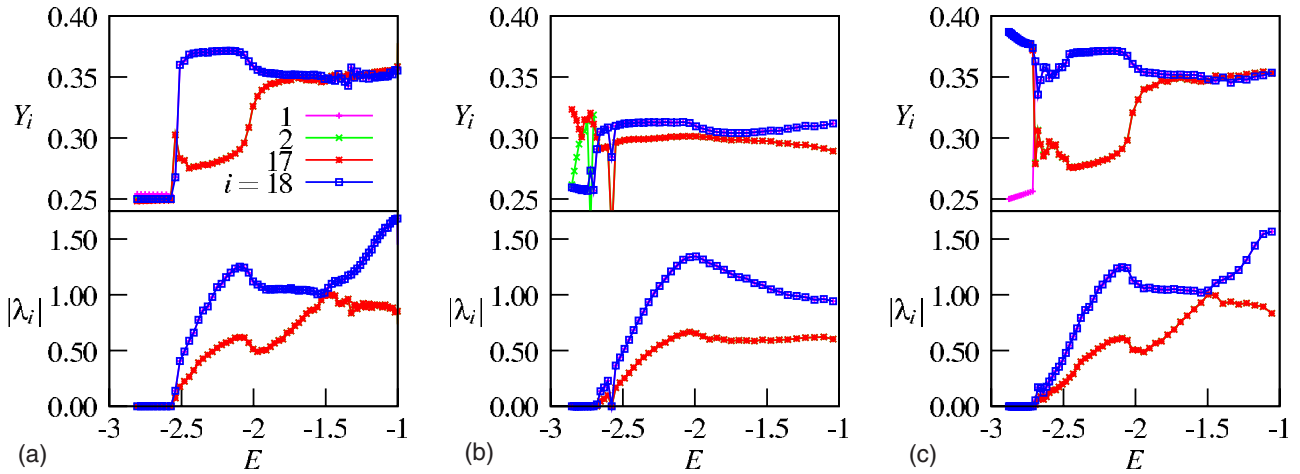


FIG. 4. (Color online) The four nonzero Lyapunov exponents  $\lambda_1=|\lambda_{18}$ ,  $\lambda_2=|\lambda_{17}$  and four inverse participation ratios  $Y_1=Y_{18}$ ,  $Y_2=Y_{17}$  as the total energy  $E$ , initially in the (a) symmetric stretch, (b) asymmetric  $E'$  mode, and (c) symmetric  $E'$  mode, of the equilateral triangle configuration is increased. The threshold energy required for chaos is greatest when the total energy is initially deposited in the symmetric stretch.  $E$  is in  $\epsilon$  units and  $\lambda$  is in natural units per reduced time.

the vertical axes. In contrast, the inverse participation ratios only increase slightly; the GSVs are similarly localized at the total energies of this region and each GSV points in largely similar directions on average along each of these trajectories. These directions must expand or contract GSVs at increasing rates with increasing total energy. At an instant, GSVs pointing in unstable directions physically represent directions with which the geometry could couple.

To gain more physical insight into the GSV directions and understand their connection to the potential-energy landscape, we may project the position vector  $\delta\mathbf{q} \in TR^{2s}$  of a GSV onto  $TR^3$  and examine the three atomic position GSVs. These three-component vectors were examined along the trajectory and compared to Figs. 1 and 3. For trajectories started from symmetrically stretched configurations, we found the position 3 vectors had relative directions similar to those of the instantaneous normal vibrational modes; atomic position vectors of  $\mathbf{g}_1$  were in asymmetric  $E'$  modelike directions and those of  $\mathbf{g}_2$  were in symmetric  $E'$  modelike directions (Fig. 5). In this context, Figs. 4(a) and 4(c) show that asymmetric  $E'$  directions are more chaotic and more localized than symmetric  $E'$  directions since  $\lambda_1 > \lambda_2$  and  $Y_1 > Y_2$ .

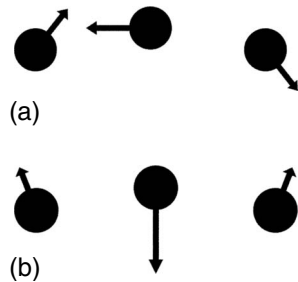


FIG. 5. Instantaneous atomic configuration and the GSV position 3 vectors of (a)  $\mathbf{g}_1$  and (b)  $\mathbf{g}_2$  in a trajectory initiated from a symmetric stretch geometry. The total energy was  $E=1.367\epsilon$ . The configuration shown was approaching and about to traverse the linear saddle.

From the trends of Fig. 4, the remaining three energy regions are defined by the approximate total energy ranges  $-2.1\epsilon < E < -1.9\epsilon$ ,  $-1.9\epsilon < E < -1.5\epsilon$ , and  $-1.5\epsilon < E < -1.0\epsilon$ . Using the terminology of Komatsuzaki *et al.*, these are the quasiregular, semichaotic, and stochastic (fully developed chaotic) regions [27]. These energy regions include motion over at least one of the linear configuration saddles, depending on which mode was initially excited. The results in these regions thus include the affect of a saddle or saddles on the long-time GSV properties. One potential-energy saddle is accessible to trajectories of initially symmetric stretch and symmetric  $E'$  configurations, while all three saddles are accessible to trajectories of initial asymmetric  $E'$  configurations.

Traversing additional saddles means different features of the potential landscape and phase space can be accessed by asymmetric  $E'$  trajectories. The results of Fig. 4(b) suggest that the GSVs for trajectories of initially asymmetric  $E'$  configurations were different. Comparing the relative directions of the position 3 vectors of  $\mathbf{g}_1$  and  $\mathbf{g}_2$  to those of the normal vibrational modes, we found that both could be identified as either symmetriclike directions or asymmetriclike  $E'$  directions in a given span of time. This finding is a consequence of motion in the potential wells off the vertical axes of Fig. 3.

At least one saddle is first accessible in the quasiregular region, being accessed more frequently as the total energy is increased. Let us consider the symmetric stretch and symmetric  $E'$  results, which are nearly identical. Again, for a physical picture, consider the representative instantaneous atomic configuration and the  $\mathbf{g}_1$  and  $\mathbf{g}_2$  position 3 vectors shown in Fig. 5. Though the configuration was initially an equilateral triangle, the symmetric stretch coupled with the symmetric  $E'$ . The configuration shown was just before traversal of the linear configuration saddle. Position 3 vectors of  $\mathbf{g}_2$  are symmetric  $E'$  modelike directions capturing directions of flux over the saddle. The three vectors of  $\mathbf{g}_1$  are asymmetric  $E'$  modelike directions capturing directions orthogonal to the flux.

With this physical picture, we see that  $\mathbf{g}_1$  directions orthogonal to the flux over the saddle are less stable and more

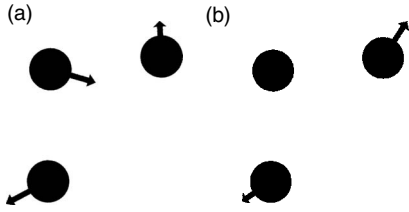


FIG. 6. Instantaneous atomic configuration and the GSV position 3 vectors of (a)  $\mathbf{g}_1$  and (b)  $\mathbf{g}_2$  in a trajectory initiated from an asymmetric  $E'$  mode geometry. The total energy was  $E=1.375\epsilon$ . The configuration shown had just traversed the linear saddle.

chaotic than the  $\mathbf{g}_2$  directions of the flux since  $\lambda_1$  is greater than  $\lambda_2$ . Both GSVs become less chaotic with increasing energy in the quasiregular region. When the trajectory spends more time on and near the saddle, the Lyapunov exponents  $\lambda_1$  and  $\lambda_2$  decrease. Decreases in  $\lambda_i$  with energy are indicative of the regularizing effect of motion across a saddle [2–5]. We also find that the inverse participation ratio  $Y_1$  decreases while  $Y_2$  increases. Thus, with increasing energy,  $\mathbf{g}_1$  directions orthogonal to the flux become more delocalized and  $\mathbf{g}_2$  directions toward the saddle become more localized.

Trajectories initiated by symmetric stretch excitations in the semichaotic energy region also lead to isomerization upon coupling with the symmetric  $E'$ ; trajectories initiated by symmetric  $E'$  excitations lead to coupling with the symmetric stretch. In this region, histories are able to more fully explore the equilateral triangle potential wells on either side of the single accessible linear saddle. As the initial energy is increased, trajectories spend increased amounts of time exploring these potential wells:  $\lambda_2$  increases and the GSV inverse participation ratios  $Y_1$  and  $Y_2$  become similarly localized but distinguishable. The increase in  $\lambda_2$  indicates that the  $\mathbf{g}_2$  GSV directions of flux over the saddle along the trajectory become increasingly chaotic. The set of directions involved and, hence, the localization, changes little because the two wells, their associated phase space, and hence their tangent spaces are identical.

Lastly, in the stochastic (fully developed chaotic) energy region  $\lambda_1$  again increases.  $\lambda_2$  plateaus, in contrast to the semichaotic region.  $\mathbf{g}_1$  has position 3 vectors that point in asymmetriclike  $E'$  directions and, hence,  $\lambda_1$  increases in response to directions in the tangent spaces associated with the potential landscape features off the vertical axis of the maps in Fig. 3. Since  $\mathbf{g}_2$  position 3 vectors are mostly in symmetriclike  $E'$  directions  $\lambda_2$  versus  $E$  plateaus. The system also spends less time traversing the saddle with increasing energy, causing  $\lambda_2$  to decrease slightly. The difference between  $Y_1$  and  $Y_2$  is small at these high energies.

Asymmetric  $E'$  excitations in the semichaotic region allow trajectories to access more than one saddle and the atomic positions to permute. Regions of phase space are explored that are unreachable in the symmetric stretch and symmetric  $E'$  trajectories. Along asymmetric  $E'$  trajectories, the position 3 vectors of  $\mathbf{g}_1$  and  $\mathbf{g}_2$  each point in more symmetriclike  $E'$  directions during some time spans and more asymmetriclike  $E'$  directions during other time spans (Fig. 6). In both the semichaotic and stochastic regions,  $Y_1$  and  $Y_2$  are smaller.  $\mathbf{g}_1$  is more delocalized than in the symmetric

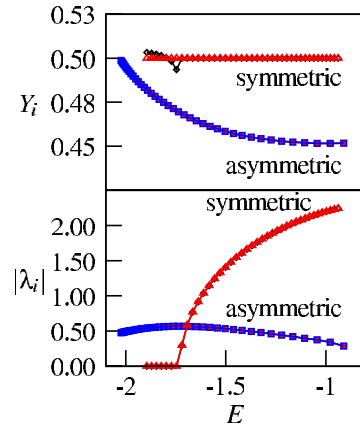


FIG. 7. (Color online) One Lyapunov exponent pair was non-zero when the total energy  $E$  was initially in the symmetric stretch of the linear configuration. Two exponent pairs were non-zero and identical when the asymmetric stretch was initially excited. The absolute values of these Lyapunov exponents and their inverse participation ratios with  $E$  are shown as a function of total energy.

stretch and symmetric  $E'$  trajectories because the symmetric  $E'$  mode occurs about each of the atoms, not just one, and also because of the different directions sampled in different time spans. The Lyapunov exponent  $\lambda_1$  shows a corresponding decrease in these energy regimes.  $\lambda_2$  increases slightly but is smaller than in Figs. 4(a) and 4(c).

Overall, the trends of Fig. 4 reflect the changes in the union of tangent spaces with increasing total energy. Lyapunov exponents  $\lambda_i$  and inverse participation ratios  $Y_i$  were both calculated from the same GSV  $\mathbf{g}_i$ . Thus, changes in  $\lambda_i$  with total energy coincide with changes in  $Y_i$ , reflecting changes in  $\mathbf{g}_i$ . Also observable from these total-energy trends is that the GSV with the largest  $\lambda_i$  generally also has the largest  $Y_i$  (i.e., it is the most localized). This result is in agreement with Forster *et al.* in their study of hard-disk fluids [42].

Briefly, we now mention global results for trajectories initiated from linear configurations. Exciting the asymmetric stretch of the linear configuration (Fig. 2), two pairs of Lyapunov exponents are non-zero, all of equal magnitude. Figure 7 shows that these trajectories were chaotic at all total energies examined. There is no coupling between the linear configuration symmetric and asymmetric modes because of symmetry. Only one pair of Lyapunov exponents is non-zero for the symmetric stretch case. The central atom is fixed at the center of mass and symmetry requirements give another zero Lyapunov exponent.

The total-energy trends of  $Y_i$  reveal GSVs for trajectories in these two cases are more localized than those for equilateral triangle trajectories, as expected, and over a wide range of energy, the GSVs for linear configuration trajectories are more localized in the symmetric stretch case than the asymmetric case. A maximum is present in the Lyapunov exponents at the total energy of asymmetric stretch case, where the symmetric stretch trajectories first become chaotic. Let us now examine the finite-time Lyapunov exponents and localization properties of the GS vectors in these energy regions over a range of time scales.

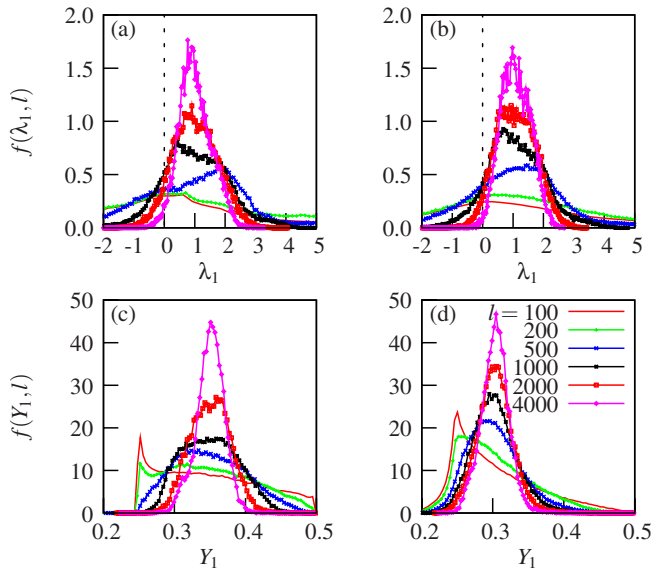


FIG. 8. (Color online) Panels (a) and (b) show  $\lambda_1$  distributions  $f(\lambda_1, l)$  for a range of time segment lengths  $l$ . Panels (c) and (d) show  $Y_1$  distributions  $f(Y_1, l)$  for a range of time segment lengths  $l$ . For (a) and (c), the total energy was initially deposited in the symmetric stretch  $E = -1.582\epsilon$ . For (b) and (d), it was deposited in the asymmetric  $E'$  mode  $E = -1.586\epsilon$ .

### B. Local properties of extended phase space

Phase-space trajectories were partitioned into segments  $\{\mathbf{x}(t_j) : 0 < j < l\}$  of equal length  $l$  to examine local properties of GSVs: a trajectory with a total length of  $L$  time steps was divided into  $L/l$  segments. A set of finite-time Lyapunov exponents and inverse participation ratios were calculated from GSVs propagated over each time segment. Finite-time Lyapunov exponents are denoted  $\{\lambda_i(\mathbf{x}_0, l)\}$  and inverse participation ratios are denoted  $\{Y_i(\mathbf{x}_0, l)\}$  to indicate their dependence on  $\mathbf{x}_0 \equiv \mathbf{x}(t_0)$ , the initial phase point of the time segment, and  $l$ , the length of the time segment. In what follows,  $\lambda_i$  and  $Y_i$  will refer to finite-time quantities. Segments of length  $l = 100, 200, 500, 1000, 2000, 4000$  gave  $L/l = (50, 25, 10, 5, 2.5, 1.25) \times 10^4$  segments for  $5 \times 10^7$  time step trajectories. Distributions  $\{f(\lambda_i, l)\}$  and  $\{f(Y_i, l)\}$ ,  $i = 1, \dots, 2s$  were generated for each partition of trajectories at each total energy.

Finite-time Lyapunov exponents quantify the average rates of expansion and contraction in the directions of the chosen vector set in each time segment: here, the GS basis vectors. As in the asymptotic limit, expanding or diverging directions have positive finite-time Lyapunov exponents ( $\lambda_1$  and  $\lambda_2$ ) and contracting or converging directions have negative finite-time Lyapunov exponents ( $\lambda_{17}$  and  $\lambda_{18}$ ). For all total energies, segment lengths, and initially excited modes,  $f(\lambda_1, l)$  and  $f(\lambda_{18}, l)$  (not shown) are symmetric about the  $\lambda = 0$  axis, as are  $f(\lambda_2, l)$  and  $f(\lambda_{17}, l)$  (not shown).

As the length  $l$  of the trajectory segments is increased the distribution of finite-time exponents narrows, eventually converging to the asymptotic value [24]. At least in part, this may be caused by expansions and contractions canceling on time scales shorter than that of the time segment [9]. Figures 8 and 9 show  $f(\lambda_1, l)$  and  $f(\lambda_2, l)$  for a range of time segment

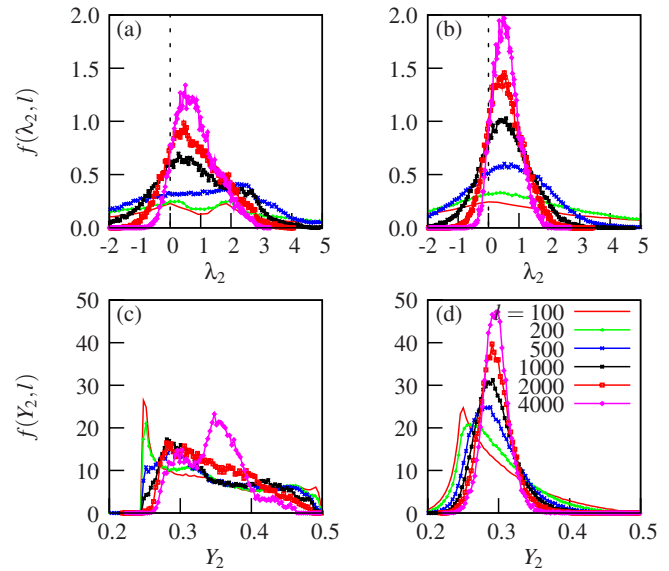


FIG. 9. (Color online) Panels (a) and (b) show  $\lambda_2$  distributions  $f(\lambda_2, l)$  for a range of time segment lengths  $l$ . Panels (c) and (d) show  $Y_2$  distributions  $f(Y_2, l)$  for a range of time segment lengths  $l$ . For (a) and (c), the total energy was initially deposited in the symmetric stretch  $E = -1.582\epsilon$ . For (b) and (d), it was deposited in the asymmetric  $E'$  mode  $E = -1.586\epsilon$ .

lengths, demonstrating this convergence. Results are shown in Figs. 8(a), 8(c), 9(a), and 9(c) for trajectories in which the symmetric stretch was initially excited to a total energy of  $E = -1.582\epsilon$ . Results for excitation of the asymmetric  $E'$  mode ( $E = -1.586\epsilon$ ) are in Figs. 8(b), 8(d), 9(b), and 9(d). The areas under these distributions are normalized to unity.

Also in Figs. 8 and 9 are  $f(Y_1, l)$  and  $f(Y_2, l)$ , distributions of the mean inverse participation ratio for each time segment length. At all total energies and time segment lengths,  $f(Y_1, l)$  and  $f(Y_{18}, l)$  (not shown) are identical, as are  $f(Y_2, l)$  and  $f(Y_{17}, l)$  (not shown). These distributions, like the exponent distributions, undergo qualitative changes over the range of time scales examined: distributions narrow for longer time segments. In finite-time segments, the value of each inverse participation ratio realization again measures the degree of GSV localization. However, measuring GSV localization for a range of segment lengths gives insight into the space and time localization of the GS basis as the history of the trajectory fills the available phase space.

Given a partitioned trajectory, GSVs may be more localized on some time segments and more delocalized on other time segments. Fluctuations in the degree of localization are reflected in the distributions  $f(Y_i, l)$ . As mentioned above, exciting the three normal modes of the equilateral triangle above the energy of the linear saddle configuration allows different regions of phase space to be accessed by trajectories. Consequently, trajectories initiated from symmetric stretch configurations at total energies above this threshold have significantly different distributions  $f(\lambda_1, l)$  and  $f(Y_1, l)$  [ $f(\lambda_2, l)$  and  $f(Y_2, l)$ ] than those for an excited asymmetric  $E'$  mode, especially for shorter time segment lengths. Distributions for trajectories with an initially excited symmetric  $E'$  mode were nearly identical to those with an initially excited

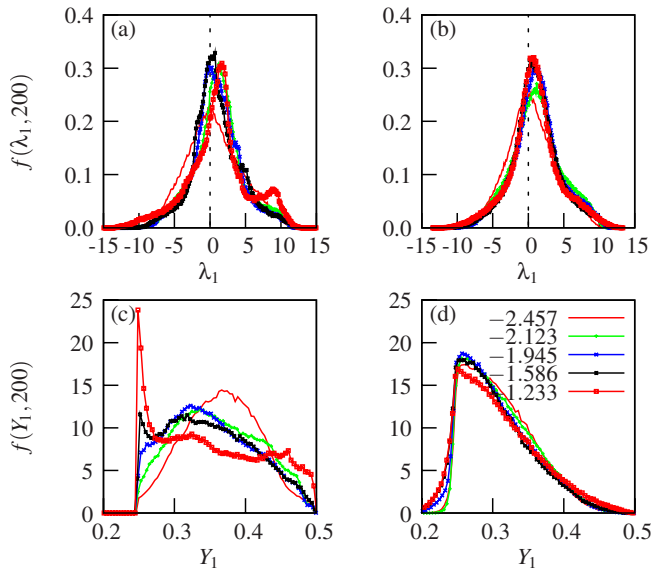


FIG. 10. (Color online) Panels (a) and (b) show  $\lambda_1$  distributions  $f(\lambda_1, 200)$  over a range of total energy. Panels (c) and (d) show  $Y_1$  distributions  $f(Y_1, 200)$  over a range of total energy. For (a) and (c), the total energy was initially deposited in the symmetric stretch, and for (b) and (d) it was deposited in the asymmetric  $E'$  mode.

symmetric stretch, so the latter distributions are not shown. The similarity of these results is a consequence of the exclusive coupling of these modes.

On shorter time scales, the distributions  $f(Y_1, l)$  are broad, reflecting GSVs in the finite-time intervals with a wide range of localization. A broad peak indicates a GSV that spends time pointing in many directions. It also indicates that a GSV has a highly variable number of components participating from segment to segment. As the time segment length  $l$  is increased,  $f(Y_i, l)$  narrow significantly. Small fluctuations about the distributions' mean suggest that less time is spent sampling some tangent space features and their GSV directions contribute little to the average properties. The most frequented directions on longer time scales are likely to be the large contributors to the global GSV properties.

At the total energy chosen for Figs. 8 and 9, the atomic configuration is able to move between the equilateral potential wells over a linear saddle in trajectories initiated from symmetric stretch or asymmetric  $E'$  configurations. The similarity of  $f(\lambda_1, l)$  distributions [and  $f(Y_1, l)$  distributions] from these trajectories for  $l > 500$  is a result of  $\mathbf{g}_1$  capturing similar directions more often on the longer time scales. In both cases, the GSV position 3 vectors are mostly asymmetriclike  $E'$  directions at this energy [Fig. 5(a)], but this is not the case at all total energies. Comparing the  $f(\lambda_2, l)$  distributions [and  $f(Y_2, l)$  distributions] from these trajectories, we see they are not similar at this energy. This difference is because  $\mathbf{g}_2$  captures symmetric  $E'$  modelike directions in the symmetric stretch trajectory, while it captures both symmetric and asymmetric  $E'$  modelike directions in the asymmetric  $E'$  trajectory [Figs. 5(b) and 6(b)].

From Fig. 9(c),  $f(Y_2, l)$  is multimodal in the symmetric stretch case at shorter times, reflecting the localization properties of the symmetriclike  $E'$  directions [Fig. 5(b)]. The

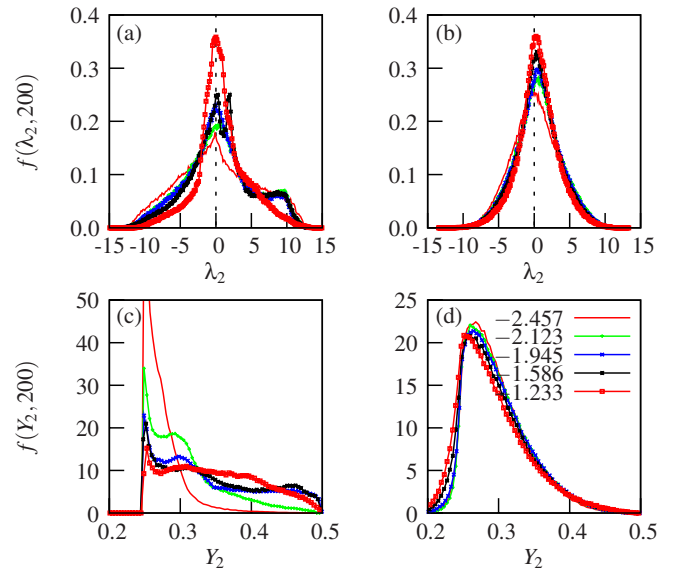


FIG. 11. (Color online) Panels (a) and (b) show  $\lambda_2$  distributions  $f(\lambda_2, 200)$  over a range of total energy. Panels (c) and (d) show  $Y_2$  distributions  $f(Y_2, 200)$  over a range of total energy. For (a) and (c), the total energy was initially deposited in the symmetric stretch, and for (b) and (d) it was deposited in the asymmetric  $E'$  mode.

multimodal nature of the  $f(\lambda_2, l)$  distribution suggests that  $\mathbf{g}_2$  directions are chaotic to varying degrees when the trajectory spends time in different regions of phase space. On shorter times, the most localized peak corresponds to symmetriclike  $E'$  directions when the configuration is near the saddle. More delocalized symmetriclike  $E'$  directions are found when the configuration is in the equilateral potential well. Since each peak may be associated with many directions, each direction having similar numbers of contributing GSV components, the number of peaks in a  $f(Y_i, l)$  distribution is only a rough indicator of the number of relevant GSV directions. Peak intensities in a distribution indicate the relative importance of each set of directions on a given time scale. We see from Fig. 9(c) that on longer time scales,  $\mathbf{g}_2$  spends more time pointing in localized directions at this total energy.

Turning to the total-energy dependence of the finite-time GSV properties, let us examine the results for  $l=200$  in Figs. 10 and 11. At energies below the saddle, the distributions of  $f(\lambda_1, 200)$  [and  $f(Y_1, 200)$ ] for different initial mode excitations are a result of  $\mathbf{g}_1$  and the accessible phase space. As mentioned, trajectories initiated from symmetric  $E'$  configurations visited a much more restricted region of phase space. The atomic position vectors of  $\mathbf{g}_1$  pointed in only asymmetriclike  $E'$  directions (Fig. 5). Trajectories initiated from asymmetric  $E'$  configurations accessed much more phase space and the position vectors of  $\mathbf{g}_1$  were aligned with symmetric or asymmetriclike  $E'$  directions, depending on the time segment and total energy (Fig. 6).

Above the total energy needed to isomerize,  $f(\lambda_1, 200)$  is bimodal as seen in Figs. 10(a) and 10(b); this result is in agreement with previous results in the region of phase space, where the linear configuration saddle can just be reached [2–5]. When the total energy is near the linear configuration potential energy,  $f(\lambda_1, 200)$  distributions develop shoulders

that are more pronounced in the symmetric stretch (and symmetric  $E'$  mode) case [Fig. 10(a)]. In Fig. 10(c),  $f(Y_1, 200)$  is broad and GSVs are more often localized at low energies. However, the distribution shifts with increasing energy, as the GSVs are more often delocalized. The distribution becomes bimodal just below the linear configuration potential energy and trimodal at energies in the semichaotic region ( $-1.9\epsilon < E < -1.5\epsilon$ ).

Consider results for trajectories initiated from symmetric  $E'$  configurations in Figs. 10(a) and 10(c). Comparing the relative peak heights in the  $f(\lambda_1, 200)$  distribution to those of the corresponding  $f(Y_1, 200)$  distribution at each total energy, we can assign exponent peaks to inverse participation ratio peaks. We assign the larger finite-time exponents to the more localized (large  $Y_1$ ) asymmetriclike  $E'$  GSV directions of  $\mathbf{g}_1$  near the linear saddle. The more delocalized GSV directions (smaller  $Y_1$ ) in the potential well or wells, we assign to the smaller finite-time exponents. GSV directions assigned to the well shift from being more localized to more delocalized as the total energy is increased because of the increased volume of phase space.

Distributions  $f(\lambda_2, l)$  and  $f(Y_2, l)$  are also multimodal over a range of total energy. Recall that the  $\mathbf{g}_2$  atomic position vectors correspond to symmetriclike  $E'$  directions [Fig. 5(b)].  $f(\lambda_2, 200)$  and  $f(Y_2, 200)$  are trimodal in a narrow energy range. One peak in  $f(\lambda_2, 200)$  is centered at zero, the other two are nonzero. The localized symmetriclike  $E'$  directions, related to the localized peaks in  $f(Y_2, 200)$ , are attached to atomic configurations with potential energies near the linear saddle. The kinetic energy in the vicinity of unstable stationary points is low when crossing is just possible, where GSVs are more localized and the instability of the region leads to large divergences of trajectories.

From Fig. 11(c), the distribution  $f(Y_2, 200)$ , in contrast to  $f(Y_1, 200)$  in Fig. 10(c), is narrow and the GSVs are more often delocalized at low energies. The distribution shifts to larger values with increasing energy as the GSVs are more often localized. Upon exceeding the potential energy of the linear configuration, both  $f(Y_1, 200)$  and  $f(Y_2, 200)$  undergo a localization-delocalization transition. The distributions  $f(Y_1, 200)$  shift from having more area localized to having more area delocalized at higher energies. This means asymmetriclike  $E'$  directions captured by  $\mathbf{g}_1$  become more localized. The distributions  $f(Y_2, 200)$  shift from being more delocalized to more localized and multimodal at higher energies as the symmetric  $E'$  modelike directions captured by  $\mathbf{g}_2$  become more localized.

#### IV. CONCLUSIONS

We have studied the tangent space directions of a full set of Gram-Schmidt vectors, simulated with trajectories of the Lennard-Jones trimer. Local and global properties were calculated for these vectors with particular interest in the case where a trajectory may fill different phase-space regions on different time scales. The degrees of stability and localization of these GSVs in finite-time spans were determined using Lyapunov exponents and inverse participation ratios. Using these GSV properties and the stationary point normal modes, we systematically probed each trajectory's approach to ergodicity at many total energies and time scales. Physical insight was gained from the atomic position components of the different GSV directions.

Multimodality in  $f(\lambda_i, l)$  distributions suggests separable time scales for the motion in different phase space and time locales, such as those regions associated with the potential wells and the linear saddles. Here we found multimodality in the distributions of the all nonzero finite-time Lyapunov exponents for some initial conditions. Multimodal distributions of inverse participation ratios collected in finite-time spans were also found. These distributions provided additional insight into the properties of the Gram-Schmidt vectors in these phase-space regions as the trimer evolved chaotically and as local ergodicity began to emerge.

The largest (finite-time) Lyapunov exponents were typically associated with the most localized GSV directions on a range of time scales. In finite-time spans, more localized GSV directions tended to be those associated with configurations near potential landscape saddles. This analysis based on a simple triatomic system is intended to be a proof-of-principle demonstration and an illustrative model. We expect the use of finite-time Lyapunov exponents and inverse participation ratios to achieve their main utility in enabling us to understand motions of somewhat larger systems.

#### ACKNOWLEDGMENTS

J.R.G. acknowledges support from the National Science Foundation (Grant No. OISE-0700911), the Argonne National Laboratory/University of Chicago Joint Theory Institute, and helpful discussions with David J. Wales. J.J. was supported by the Office of Basic Energy Sciences, Division of Chemical Sciences, Geosciences, and Biosciences, U.S. Department of Energy under Contract No. DE-AC-02-06CH11357.

[1] R. MacKay, J. Meiss, and I. Percival, *Physica D* **13**, 55 (1984).  
 [2] T. L. Beck, D. M. Leitner, and R. S. Berry, *J. Chem. Phys.* **89**, 1681 (1988).  
 [3] C. Amitrano and R. S. Berry, *Phys. Rev. Lett.* **68**, 729 (1992).  
 [4] C. Amitrano and R. S. Berry, *Z. Phys. D: At., Mol. Clusters* **26**, 388 (1993).

[5] C. Amitrano and R. S. Berry, *Phys. Rev. E* **47**, 3158 (1993).  
 [6] J.-P. Eckmann and D. Ruelle, *Rev. Mod. Phys.* **57**, 617 (1985).  
 [7] P. Brumer and J. W. Duff, *J. Chem. Phys.* **65**, 3566 (1976).  
 [8] R. Kosloff and S. A. Rice, *J. Chem. Phys.* **74**, 1947 (1981).  
 [9] D. J. Wales and R. S. Berry, *J. Phys. B* **24**, L351 (1991).  
 [10] B. Eckhardt and D. Yao, *Physica D* **65**, 100 (1993).  
 [11] R. J. Hinde, D. J. Wales, and R. S. Berry, *J. Chem. Phys.* **96**,

- 1376 (1992).
- [12] M. A. Sepúlveda, R. Badii, and E. Pollak, *Phys. Rev. Lett.* **63**, 1226 (1989).
- [13] A. Battisti, R. G. Lalopa, A. Tenenbaum, and M. D'Alessandro, *Phys. Rev. E* **79**, 046206 (2009).
- [14] R. Bell, P. Dean, and D. Hibbins-Butler, *J. Phys. C* **3**, 2111 (1970).
- [15] G. Benettin, L. Galgani, A. Giorgilli, and Jean-Marie Strelcyn, *Meccanica* **15**, 9 (1980).
- [16] G. Benettin, L. Galgani, A. Giorgilli, and J.-M. Strelcyn, *Mecchanica* **15**, 21 (1980).
- [17] S. V. Ershov and A. B. Papatov, *Physica D* **118**, 167 (1998).
- [18] B. Legras and R. Vautard, in *1995 ECMWF Seminar on Predictability*, edited by T. Palmer (ECMWF, Reading, UK, 1996), pp. 143–156.
- [19] A. Trevisan and F. Pancotti, *J. Atmos. Sci.* **55**, 390 (1998).
- [20] C. L. Wolfe and R. M. Samelson, *Tellus, Ser. A* **59A**, 355 (2007).
- [21] F. Ginelli, P. Poggi, A. Turchi, H. Chaté, R. Livi, and A. Politi, *Phys. Rev. Lett.* **99**, 130601 (2007).
- [22] H.-L. Yang and G. Radons, *Phys. Rev. E* **71**, 036211 (2005).
- [23] G. Radons and H.-L. Yang, *Static and Dynamic Correlations in Many-Particle Lyapunov Vectors* (2004) (<http://arxiv.org/abs/nlin/0404028>).
- [24] H. Abarbanel, R. Brown, and M. Kennel, *J. Nonlinear Sci.* **1**, 175 (1991).
- [25] V. I. Oseledec, *Trans. Mosc. Math. Soc.* **19**, 197 (1968).
- [26] R. J. Hinde and R. S. Berry, *J. Chem. Phys.* **99**, 2942 (1993).
- [27] T. Komatsuzaki and R. S. Berry, *Proc. Natl. Acad. Sci. U.S.A.* **98**, 7666 (2001).
- [28] D. J. Wales, *Energy Landscapes* (Cambridge University Press, England, 2003).
- [29] S. Chekmarev and F. Liu, *Z. Phys. D: At., Mol. Clusters* **20**, 231 (1991).
- [30] E. Yurtsever and N. Elmaci, *Phys. Rev. A* **55**, 538 (1997).
- [31] E. Yurtsever, *Phys. Rev. A* **58**, 377 (1998).
- [32] E. D. Belega, D. N. Trubnikov, and L. L. Lohr, *Phys. Rev. A* **63**, 043203 (2001).
- [33] A. Rybakov, E. D. Belega, and D. Trubnikov, *Eur. Phys. J. D* **41**, 297 (2007).
- [34] F. Calvo, *J. Chem. Phys.* **108**, 6861 (1998).
- [35] W. C. Swope, H. C. Andersen, P. H. Berens, and K. R. Wilson, *J. Chem. Phys.* **76**, 637 (1982).
- [36] L. Verlet, *Phys. Rev.* **159**, 98 (1967).
- [37] A. Iserles, *A First Course in the Numerical Analysis of Differential Equations*, Cambridge Texts in Applied Mathematics, 2nd ed. (Cambridge University Press, England, 2008).
- [38] H.-D. Meyer, *J. Chem. Phys.* **84**, 3147 (1986).
- [39] H. A. Posch and W. G. Hoover, *Phys. Rev. A* **39**, 2175 (1989).
- [40] F. Bonetto, E. Cohen, and C. Pugh, *J. Stat. Phys.* **92**, 587 (1998).
- [41] A. Pikovsky and A. Politi, *Nonlinearity* **11**, 1049 (1998).
- [42] C. Forster, R. Hirschl, H. A. Posch, and W. G. Hoover, *Physica D* **187**, 294 (2004).